An Investigation of Real Gas Effects in Supercritical CO_2 Centrifugal Compressors

Nikola D. Baltadjiev
MIT Gas Turbine Laboratory,
Massachusetts Institute of Technology,
Cambridge, MA 02139
e-mail: nikola@alum.mit.edu

Claudio Lettieri
MIT Gas Turbine Laboratory,
Massachusetts Institute of Technology,
Cambridge, MA 02139
e-mail: lettieri@mit.edu

Zoltán S. Spakovszky
MIT Gas Turbine Laboratory,
Massachusetts Institute of Technology,
Cambridge, MA 02139
e-mail: zolti@mit.edu

This paper presents a comprehensive assessment of real gas effects on the performance and matching of centrifugal compressors operating in supercritical CO_2. The analytical framework combines first principles based modeling with targeted numerical simulations to characterize the internal flow behavior of supercritical fluids with implications for radial turbomachinery design and analysis. Trends in gas dynamic behavior, not observed for ideal fluids, are investigated using influence coefficients for compressible channel flow derived for real gas. The variation in the properties of CO_2 and the expansion through the vapor-pressure curve due to local flow acceleration are identified as possible mechanisms for performance and operability issues observed near the critical point. The performance of a centrifugal compressor stage is assessed at different thermodynamic conditions relative to the critical point using computational fluid dynamics (CFD) calculations. The results indicate a reduction of 9% in the choke margin of the stage compared to its performance at ideal gas conditions due to variations in real gas properties. Compressor stage matching is also impacted by real gas effects as the excursion in corrected mass flow per unit area from inlet to outlet increases by 5%. Investigation of the flow field near the impeller leading edge at high flow coefficients shows that local flow acceleration causes the thermodynamic conditions to reach the vapor-pressure curve. The significance of two-phase flow effects is determined through a nondimensional parameter that relates the time required for liquid droplet formation to the residence time of the flow under saturation conditions. Applying this criterion to the candidate compressor stage shows that condensation is not a concern at the investigated operating conditions. In the immediate vicinity of the critical point however, this effect is expected to become more prominent. While the focus of this analysis is on supercritical CO_2 compressors for carbon capture and sequestration (CCS), the methodology is directly applicable to other nonconventional fluids and applications. [DOI: 10.1115/1.4029616]

Introduction

Despite efforts to utilize reusable energy sources, such as wind and solar power, fossil fuels remain the primary source of energy worldwide. Coal-burning power plants produce nearly 40% of carbon dioxide emissions worldwide and even a larger percentage is registered in growing countries [1]. One way to reduce the negative impact on the environment is by means of CCS. In this process, CO_2 is captured before being released into the atmosphere, compressed to very high pressures reaching supercritical state, and injected deep underground into saline aquifers or coal beds. At this state, the fluid has density of a liquid and viscosity of a gas. This makes it a suitable working fluid for extracting natural gas and oil in enhanced oil recovery (EOR), yielding 50% more oil than standard methods using air and water. Retrofitting plants with CCS systems, however, is costly and power requirements can reach up to 20% of the plant gross power output [2]. In the U.S. alone, more than 5 billion tons of CO_2 per year are released into the atmosphere [1]. Given the enormous scale of these applications, efficiency levels can have a dramatic impact on operating costs and profits. Moreover, it is common practice in industry to adapt existing turbomachinery to these applications rather than analyzing the particular features of these unconventional working fluids. The resulting compressor stages tend to have very low efficiency levels and there is experimental evidence for unstable behavior when approaching the critical point [3]. The limitations of typical S-CO_2 compressor designs used in industry have been identified in the literature, see, for example, Ref. [4], and are associated with increased aerodynamic losses at low-flow-coefficients. This paper focuses exclusively on the assessment of real gas effects on the performance and matching of compressor stages.

While much research has been done on characterizing the state of supercritical fluids, the fluid dynamic effects of supercritical CO_2 on turbomachinery internal flow are still largely unknown. A study by Luüdtke [5] compares three of the most common real gas models: the Benedict, Webb, and Rubin formulation with extension by Sterling referred to as the BWRS model, the formulation by Redlich and Kwong augmented by Soave known as the RKS model, and the Lee and Kesler (LK) model modified by Ploker, Knapp, and Prausnitz referred to as the LKP model. Compressibility factors calculated using these models were compared against gas property tables published in the 1960s and 1970s for selected fluids. The study found that for CO_2 at pressures between 50 bar and 250 bar the LKP model had the best agreement with experimental data, with deviation of less than 2%. The BWRS model had significantly worse agreement of up to 5%, while the RKS model was not recommended at all. A more recent equation of state (EOS) model, particularly tailored for carbon dioxide, was developed by Span and Wagner (SW) [6] whose accuracy is shown to be on the same order as the uncertainty of the experimental measurements, which is 0.05% for density. The LK model is well-established and widely used in industry, while the SW model has recently gained popularity, mainly in science and research, due to emerging new applications for supercritical CO_2. Current practice employs standard design tools for conventional fluids coupled with thermodynamic property models to analyze the performance and the matching of centrifugal compressor stages operating in supercritical CO_2. In this, a clear description and characterization of the real gas effects of the fluid on the internal flow behavior and related mechanisms is missing.

Contributed by the International Gas Turbine Institute (IGTI) of ASME for publication in the JOURNAL OF TURBOMACHINERY. Manuscript received December 17, 2014; final manuscript received December 28, 2014; published online February 25, 2015. Editor: Ronald Bunker.

Recently, efforts are also aimed at improving the compression process to reduce the power requirements of supercritical CO_2 compressors. For example, Moore and Nored [7] propose a quasi-isothermal compression process using intercooling between each centrifugal stage to improve efficiency. This approach, however, adds significant complexity to the system and leads to potential reliability risks. The development of an internally cooled centrifugal compressor is presented in Ref. [8], where a cooling jacket is embedded around the gas flow path. The experimental results from a single stage test rig show that over 50% of the heat addition by the impeller can be removed. The feasibility of this concept in a multistage configuration at supercritical pressures has yet to be demonstrated. An alternative method is to liquefy the CO_2 after the first vapor compression and to use cryogenic liquid pumps to reach supercritical pressure. The combined power requirement for refrigeration and pumping is much lower than for the pure vapor compression, but there are significant system level challenges such as the less efficient transport of liquid CO_2.

Supercritical CO_2 is also being considered for Brayton cycle applications [9–11] as the liquidlike density and specific heat capacity of the fluid can potentially increase the power conversion efficiency. Test loops to demonstrate the feasibility of the concept and to investigate the system performance and characteristics are operated at Sandia National Laboratory [3]. The turbomachinery specifications are presented in Fuller et al. [12], and a two-dimensional turbomachinery through-flow model is proposed by Lee et al. [13]. To establish the stage geometry and the performance maps, different empirical loss models developed for conventional turbomachinery are combined with a real gas EOS. In this, the direct impact of the real gas effects on the different loss mechanisms is neglected. Pecnik et al. [14] present a numerical simulation of a CO_2 centrifugal compressor stage operating in the vicinity of the critical point. The main focus is on validating the numerical schemes and the interaction between the solver and the real gas model.

Scope of Paper

While a great deal of work has been carried out on characterizing the thermodynamic real gas state, very little is known about the internal flow behavior of supercritical CO_2 in fluid machinery. There is evidence that the performance can be greatly limited and that serious operability issues can occur when operating CO_2 compressors at supercritical conditions near the critical point. The aim of this paper is to rigorously characterize the impact of real gas behavior on turbomachinery internal flow when operating closer and closer to the critical point as illustrated in Fig. 1.

More specifically, the objectives of the paper are to: (1) quantify the limitations of ideal gas based turbomachinery through-flow analysis at supercritical conditions but away from the critical point, (2) quantify in a rigorous manner the real gas effects on compressible flow and gas dynamic behavior near the critical point, and (3) investigate the root cause and mechanisms responsible for the compressor performance and operability issues. It will be shown that, when approaching the critical point, variations in compressibility and isentropic exponents can significantly impact the compressor stage matching. Further, while the thermodynamic state properties can exhibit large changes, the fundamental derivative of CO_2 (the curvature of the isentrope in p-v coordinates) remains positive away from the critical point, indicating that possible inversion of gas dynamic effects is not a concern. However, near compressor choke, shock-induced separation can lead to a Kelvin–Helmholtz type flow instability. Condensation and CO_2 liquid droplet formation can occur in the compressor blade passage due to local flow acceleration. To address these issues, the technical approach combines one-dimensional gas dynamic analysis using corrected flow and influence coefficients with two-dimensional numerical simulations of canonical internal flow situations and three-dimensional, unsteady real gas calculations of a representative centrifugal compressor stage approaching the critical point. Detailed T-s diagrams representing the real gas thermodynamic properties of CO_2 are provided in the Appendix.

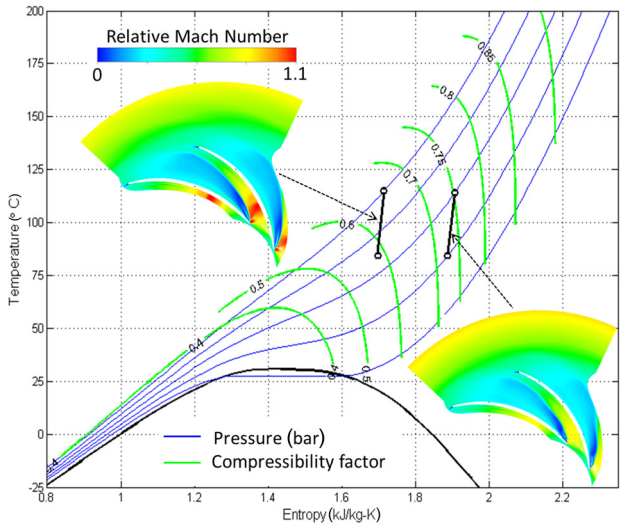

Fig. 1 Focus of paper is the in-depth assessment of internal flow behavior as the critical point is approached

Numerical Methods

The commercial solver ANSYS CFX 14 [15] was used for all computations in this paper. The computational method is based on a finite-volume approach using an implicit compressible formulation with second order spatial discretization. The Reynolds-averaged Navier–Stokes equations are closed through the two-equation k-ω shear stress transport turbulence model.

Due to the large variations in thermodynamic properties of supercritical CO_2, special care was taken in maintaining numerical stability. The locations of the inlet and exit boundaries were chosen so as to avoid any boundary interference. The Courant–Friedrich–Lewy (CFL) number in the steady calculation was decreased below 1 when approaching the critical point, while the acoustic CFL number was kept close to unity. In the unsteady calculations near the critical point, refined time steps were required to maintain the acoustic CFL number below unity, leading to a time step on the order of 10^{-7} s. The total pressure was defined at the inlet boundary with the flow velocity normal to the boundary.

The compressor stage Reynolds number is on order of 10^7, and careful grid refinements near the endwalls and blade boundaries were required to accurately capture the friction losses. Grid convergence was achieved demonstrating less than 1% change in velocity, pressure and temperature profiles, and no appreciable difference in polytropic efficiency and pressure coefficient. The wall roughness was set to an equivalent sand grain roughness of $0 \leq h^+_s \leq 5$, representative of a highly polished smooth surface. For all calculations, the average $y+$ value was kept close to unity with at least 13 mesh cells in the boundary layer. The maximum $y+$ was about 20, which was reached only in regions with large local overspeed such as near the impeller leading edge. The total number of grid points for a single passage calculation amounted to 2×10^6. The convergence criteria of the calculation were based on the reduction of RMS momentum and energy residuals below 10^{-5} and RMS of residuals of mass, stage polytropic efficiency, and pressure coefficient below 10^{-6}.

The LK and SW real gas EOS models were identified as the most suitable EOS models for the range of thermodynamic conditions of interest. The LK model is based on the three-parameter corresponding states principle, where data from several different fluids are used to develop a general correlation that is applicable over a wide range of states. Its main drawback is the diminishing accuracy in the vicinity of the critical point, particularly in the

derived properties. The SW model on the other hand is developed specifically for CO_2. The empirical correlation is optimized to fit experimental measurements of p-v-T data, enthalpy, entropy, speed of sound, and other properties. Special treatment of the critical region is considered to ensure that the highly nonlinear behavior of the fluid in that region is captured appropriately. Comparison of the two EOS models shows that they are in good agreement in the vicinity of the compressor operating range. The average relative error in the LK model compared to the SW is found to be less than 1% in the primary properties, such as density, and less than 2.5% in the derived properties, such as c_p. For simulations that extend closer to the critical point, however, the SW EOS model should be used.

NIST's formulation of the SW EOS model, part of REFPROP [16], was adopted and incorporated in the CFD solver in the form of lookup tables. The implementation was tested and validated through a systematic refinement of the lookup table. It was found that for the pressure and temperature range of interest there was no appreciable difference in compressor polytropic efficiency and pressure coefficient if the table entries were resolved within 0.1 K in temperature and 0.1 bar in pressure. Two-phase calculations were conducted using a user-defined model for droplet nucleation and growth, based on classical nucleation theory and under the assumptions of heterogeneous nonequilibrium condensation. More detail is given later, in the Condensation Effects section.

Real Gas Aerothermodynamics

The nonideal state of a fluid gives rise to a set of derived properties that impact the governing equations of compressible flow for real gas. Studying the behavior of these properties can help identify various real gas phenomena and provide insight into the operation of a compressor stage. One such property is the compressibility factor (Z), which can be interpreted as the deviation of a fluid's real specific volume from the one predicted by ideal gas theory. The value of Z, however, only gives the magnitude of this deviation, while the gradients of Z with respect to pressure and temperature determine the behavior of the fluid in thermodynamic processes. These secondary properties can be related to the isothermal and isobaric compressibilities of a fluid by the relationships

$$\beta_T = -\frac{1}{v}\left(\frac{\partial v}{\partial p}\right)_T = \frac{1}{p} - \frac{1}{Z}\left(\frac{\partial Z}{\partial p}\right)_T \tag{1}$$

$$\beta_p = \frac{1}{v}\left(\frac{\partial v}{\partial T}\right)_p = \frac{1}{T} + \frac{1}{Z}\left(\frac{\partial Z}{\partial T}\right)_p \tag{2}$$

Using Eqs. (1) and (2), the caloric EOS for a real gas in terms of $h(T,p)$ and $u(T,v)$ can be written as

$$dh = c_p dT + v(1 - \beta_p T)dp \tag{3}$$

$$du = c_v dT + p\left(\frac{\beta_p T}{\beta_T p} - 1\right)dv \tag{4}$$

These relationships indicate that whenever Z is not constant both the enthalpy and the internal energy of a real gas no longer depend only on temperature. This has important implications in the derivation of the isentropic relations for real gas. The expressions for the isentropic exponents n_s and m_s can be written as

$$n_s = -\frac{v}{p}\left(\frac{\partial p}{\partial v}\right)_s = \frac{\gamma}{\beta_T p} \tag{5}$$

$$m_s = \frac{p}{T}\left(\frac{\partial T}{\partial p}\right)_s = \frac{\gamma - 1}{\gamma}\frac{\beta_T p}{\beta_p T} \tag{6}$$

Detailed derivations of all equations presented here can be found in Ref. [17]. Another important deviation from ideal gas theory is observed in the expression for speed of sound for a real gas. Substituting Eq. (5) in the definition of speed of sound yields

$$a^2 = \left(\frac{\partial p}{\partial \rho}\right)_S = -v^2\left(\frac{\partial p}{\partial v}\right)_S = n_s pv = n_s ZRT \tag{7}$$

While analogous to the equations for an ideal gas, the relationships for a real fluid presented so far emphasize the importance of the gradients of the compressibility factor through the isentropic exponents. This analogy can be further extended to the relationships between static and stagnation properties. The caloric EOS can be integrated for a reversible process under the assumption that n_s and m_s remain constant between total and static conditions (equivalent to the assumption of constant γ for ideal gas). Away from the critical point, the variations in the isentropic exponents are small enough such that an average value between total and static conditions can be used as an approximation. The validity of this assumption when approaching the critical point will be further examined on a canonical test case. The integration of Eqs. (3) and (4) is described in detail in Ref. [17], and only the final results are presented here:

$$\frac{p_t}{p} = \left(1 + \frac{n_s - 1}{2}M^2\right)^{n_S/(n_S-1)} \tag{8}$$

$$\frac{T_t}{T} = \left(1 + \frac{n_S - 1}{2}M^2\right)^{m_S n_S/(n_S-1)} \tag{9}$$

$$\frac{\rho_t}{\rho} = \left(1 + \frac{n_S - 1}{2}M^2\right)^{\frac{1}{n_S-1}} \tag{10}$$

The compressible flow relationships for a real fluid follow the same form as their ideal gas equivalents, when the general form of the isentropic exponent is used in the derivations. As a result of the pressure dependency of enthalpy, the temperature ratio also features an exponent which reduces to unity in the case of an ideal fluid. Combining Eqs. (8)–(10) with the real gas EOS yields another useful relationship for the ratio of the stagnation and static compressibility factor

$$\frac{Z_t}{Z} = \left(1 + \frac{n_s - 1}{2}M^2\right)^{1-\frac{m_S n_S}{n_S-1}} \tag{11}$$

Substituting the compressible flow relations into the one-dimensional form of the continuity equation and rearranging the terms yields a general form of the corrected mass flow function

$$\frac{\dot{m}\sqrt{Z_t RT_t}}{Ap_t\sqrt{n_s}} = M\left(1 + \frac{n_S - 1}{2}M^2\right)^{(-n_S-1)/2(n_S-1)} \tag{12}$$

The real gas compressible flow analysis can be further extended to assess the effects of area change and shaft work on one-dimensional internal flow situations. Following the analysis by Greitzer et al. [18] for an ideal gas, the differential form of the governing equations of fluid motion and EOS yield a system of equations that relates the flow field variables dc/c, dT/T, dp/p, and $d\rho/\rho$ to the change in area dA/A and shaft work input $dw_{\text{shaft}}/(c_pT)$. Other derived quantities such as da/a and dM/M can be obtained by considering the definition of speed of sound and Mach number. The system can be set up as a matrix of influence coefficients, shown in Table 1.

The dependent variables from the first column can be obtained by summing the product of the influence coefficients from the corresponding row with the independent variables at the top of the column. Detailed derivation of all the terms can be found in Ref. [17]. A similar matrix assessing the effects of heat addition and friction are presented by Cheng et al. [19], although the

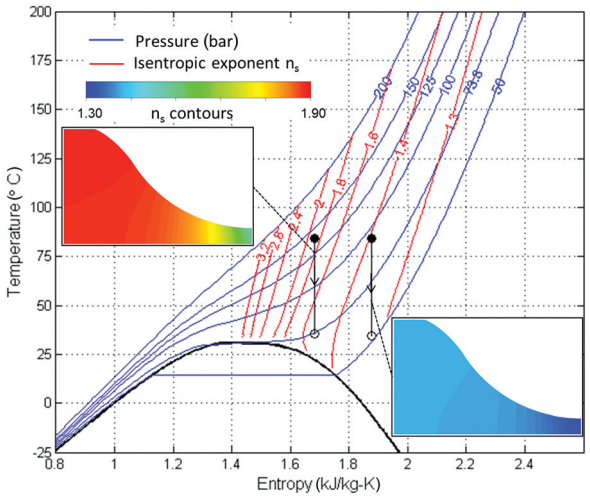

Fig. 2 Isentropic real gas expansion in a two-dimensional convergent nozzle

choice of compressibility functions is significantly different. An important thermodynamic property is the fundamental derivative, Γ, which can be related to the curvature of the isentrope in p-v coordinates through the expression

$$\Gamma = 1 + \frac{\rho}{a}\left(\frac{\partial a}{\partial \rho}\right)_S = \frac{v^3}{2a^2}\left(\frac{\partial^2 p}{\partial v^2}\right)_S \tag{13}$$

For an ideal gas, Eq. (13) reduces to $\Gamma = (\gamma + 1)/2$ and is always greater than one. Some dense gases however are known to have regions at supercritical and near critical state where the fundamental derivative becomes negative. Under this condition, a complete inversion of gas dynamic behavior is observed, where for an expanding flow the speed of sound of the fluid will increase faster than its velocity causing the Mach number to decrease. The reverse process also occurs for in an isentropic compression. This phenomenon has been extensively studied by Thompson [20]. The fundamental derivative can be estimated by using a central difference scheme to calculate derivatives of the speed of sound with respect to temperature and pressure. The fundamental derivative of CO_2 was computed using the LK EOS model and is plotted on a T-s diagram in Fig. 21 in the Appendix. While accurate estimation of Γ could not be obtained in the immediate vicinity of the critical point due to the uncertainty in speed of sound, the results suggest that inversion of gas dynamic effects is not a concern away from the critical point where current supercritical CO_2 compressors operate.

The validity of the assumption used to derive the compressible flow relations can be assessed by examining the behavior of the isentropic exponent on a T-s diagram. Near the critical point of CO_2, the isentropic exponent exhibits a strong gradient along an isotherm. As the value of n_s approaches 1.4, the value for ideal gas air, its gradient is significantly reduced. A two-dimensional converging nozzle is used to assess the error in corrected mass flow per unit area due to the variation of n_s in two expansion processes shown in Fig. 2.

The stagnation conditions of the first process, representative of a supercritical CO_2 compressor stage, are $p_t = 93.5$ bar and $T_t = 84\,^{\circ}$C, where the variation in n_s is only 6%. The second process is closer to the critical point and expands from the same stagnation temperature but from a higher stagnation pressure of 140 bar, such that an expansion to sonic conditions does not reach the two-phase region. The value of the isentropic exponent at the stagnation conditions increases to 1.9 and varies by up to 20%. Several other properties of CO_2, including m_s, compressibility factor Z, and compressibility functions $\beta_p T$ and $\beta_T p$, are also represented on T-s diagrams in the Appendix.

Table 1 Influence coefficients for real gas compressible channel flow

	$\frac{dA}{A}$	$\frac{dw_{\text{shaft}}}{c_p T}$
$\frac{dc}{c}$	$-\frac{1}{(1-M^2)}$	$\frac{1}{(1-M^2)}\frac{(\beta_p T)^2}{(\gamma-1)}$
$\frac{dT}{T}$	$\frac{M^2}{(1-M^2)}\frac{(\gamma-1)}{\beta_p T}$	$-\frac{\beta_p T}{(1-M^2)}$
$\frac{dp}{p}$	$\frac{\gamma M^2}{(1-M^2)}\frac{1}{\beta_T p}$	$-\frac{1}{(1-M^2)}\frac{\gamma}{(\gamma-1)}\frac{(\beta_p T)^2}{(\beta_T p)}$
$\frac{d\rho}{\rho}$	$\frac{M^2}{(1-M^2)}$	$-\frac{1}{(1-M^2)}\frac{(\beta_p T)^2}{(\gamma-1)}$
$\frac{dM}{M}$	$-\frac{1+(\Gamma-1)M^2}{(1-M^2)}$	$\frac{\Gamma}{(1-M^2)}\frac{(\beta_p T)^2}{(\gamma-1)}$
$\frac{da}{a}$	$\frac{(\Gamma-1)M^2}{(1-M^2)}$	$\frac{(\Gamma-1)}{(1-M^2)}\frac{(\beta_p T)^2}{(\gamma-1)}$

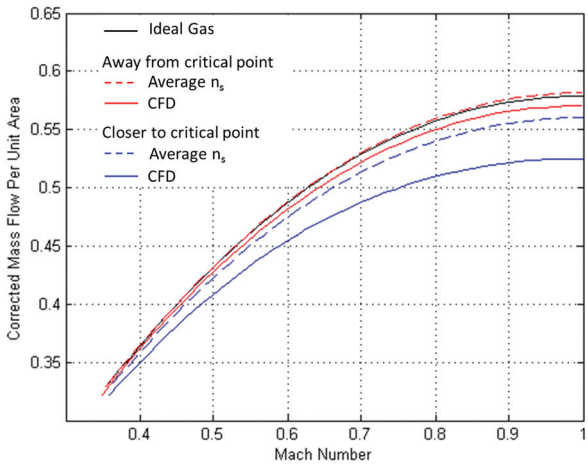

Fig. 3 Real gas effect on corrected flow per unit area

To obtain the actual value of the corrected mass flow function at the nozzle outlet, given by the left hand side of Eq. (12), CFD simulations are performed for several different pressure ratios up to choke. A free-slip, adiabatic boundary condition is applied to the nozzle wall to achieve isentropic flow. An average value of n_s between inlet and outlet is used with the right hand side of Eq. (12) to estimate the corrected mass flow per unit area with the compressible flow relations derived for real gas. The results for the two cases are plotted against outlet Mach number in Fig. 3. The corrected mass flow function for ideal gas air is also shown as a reference.

For the lower pressure case (red), the relative error between CFD (solid) and Eq. (12) (dashed) is about 1% at M = 1. The relative error for the case closer to the critical point (blue) increases up to 7%. The implications are that away from the critical point, real gas effects do not impact compressor performance significantly since the gradients in both n_s and Z (shown in Fig. 1), are nearly orthogonal to the process. The shift in the corrected mass flow function as the critical point is approached, however, implies that the compressor may choke sooner than expected, altering the matching of the compressor stages.

Stage Matching in Supercritical CO_2

A small perturbation in the inlet conditions to the first stage of a multistage compressor can yield large excursion in operating conditions of the last stage deteriorating performance and possibly

leading to surge and/or rotating stall. This effect can be assessed by examining the change in corrected mass flow per unit area through the compressor stage. First, a canonical test case is investigated, comparing the performance of a two-dimensional radial impeller operating with ideal gas air, ideal gas CO_2, and real gas CO_2. This impeller is used to investigate stage matching in supercritical CO_2 without the complexity of three-dimensional flow features and endwall effects. To preserve dynamic similarity, the same range of flow coefficients (ϕ) at the same machine Mach number (M_{U2}) was investigated for the different cases. The results were compared on the basis of polytropic efficiency and pressure coefficient, following the polytropic analysis of Schultz [21]. For all two-dimensional impeller simulations, the machine Mach number is set to 0.75. The only nondimensional parameter, which is varied between the different cases, is the stage Reynolds number. A summary of the four different test cases and the respective Reynolds numbers is presented in Table 2.

The specific heat ratio for ideal gas air was kept constant at 1.4, while that of CO_2 was modeled as a polynomial function of temperature given in Ref. [22]. The real gas CO_2 was modeled with the LK EOS. The specified temperature and pressure are representative of the inlet conditions to the first stage of the last block of an actual CO_2 compressor in service. The 2D blade profile is derived from the radial part of the original 3D blade, preserving the blade metal angle, the radial location of the trailing edge, and the blade passage periodicity of 36 deg. The 2D stage also includes the vaneless space extending up to the cross-over bend. The geometry of the stage, along with the flow field at the maximum efficiency flow coefficient for the real gas case, is shown in Fig. 4.

At these conditions, the gradient of the compressibility factor for the real gas case is nearly orthogonal to the compression process, suggesting that real gas effects do not have a significant impact on the performance of the stage. The difference in the Reynolds numbers between the ideal and real gas cases is up to 2 orders of magnitude, but since the only loss source in this test case is the profile loss, only a weak Reynolds number effect is observed in the polytropic efficiency of the stage, as shown in Fig. 5. The excursion in corrected mass flow is shown in Fig. 6, by plotting the pressure coefficient against the normalized mass flow function at the stage inlet and outlet for the four cases. While the real gas inlet and outlet corrected mass flow functions are slightly shifted due to the smaller range of flow coefficients investigated, the excursion in corrected mass flow from inlet to outlet between the four cases is nearly identical.

Table 2 2D radial impeller simulation matrix

	Fluid	Inlet condition	Re number
1	Ideal gas air	Atmospheric	10^5
2	Ideal gas air	$T_t = 55\,^{\circ}\mathrm{C}$, $p_t = 68.3$ bar	5×10^6
3	Ideal gas CO_2	$T_t = 55\,^{\circ}\mathrm{C}$, $p_t = 68.3$ bar	5×10^6
4	Real gas CO_2	$T_t = 55\,^{\circ}\mathrm{C}$, $p_t = 68.3$ bar	10^7

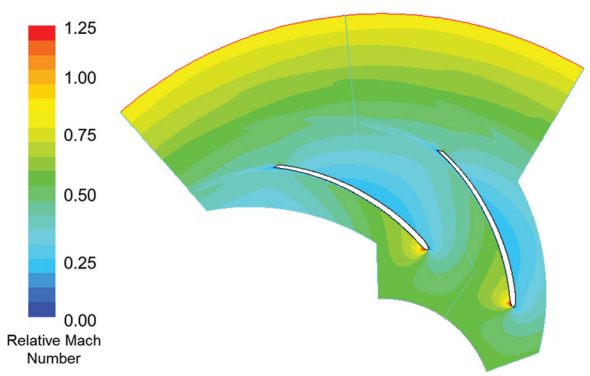

Fig. 4 2D radial impeller flow field at $M_{U2} = 0.75$ and design flow coefficient for real gas CO_2

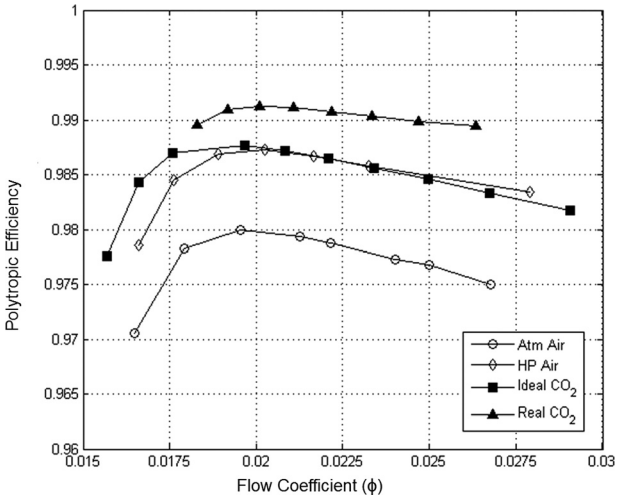

Fig. 5 Polytropic efficiency of the 2D radial impeller at $M_{U2} = 0.75$

This indicates that real gas effects have little impact on stage matching away from the critical point. Since the gradients of the compressibility factor are almost orthogonal to the compression process, the value of Z changes by about 2% from inlet to outlet of the stage. For such a small variation, the performance of the stage can be accurately modeled with the ideal gas approximation provided that dynamic similarity is preserved.

At high flow coefficients, the impeller is subjected to large negative incidence at the leading edge as the stagnation point moves toward the blade suction side. The resulting local flow acceleration causes a decrease in the static pressure and temperature of the fluid. For a real gas, the fluid state eventually falls below the saturation line, suggesting the possibility of condensation in the compressor blade passage. Approaching the critical point increases the possibility of condensation in addition to the larger variations in thermodynamic properties. These effects are studied independently through CFD simulations of the CO_2 compressor stage shown in Fig. 7.

The stage consists of a shrouded impeller followed by a vaneless diffuser and a cross-over bend. At the exit of the vaneless diffuser, the flow is decelerated below $M = 0.3$ so that the flow in the downstream components can be considered incompressible. More detail of the compressor design and configuration can be found in Ref. [4]. The stage inlet pressure is 68 bar, the machine Mach number is 0.75, the flow coefficient is below 0.01, and the impeller inlet to outlet radius ratio is 0.44.

To investigate the stage matching closer to the critical point, the compressor inlet conditions are varied similarly to the 2D nozzle study shown in Fig. 2. The inlet conditions for the baseline case are $p_t = 93.5$ bar and $T_t = 84\,^{\circ}\mathrm{C}$, providing sufficient margin from the two-phase region. The critical point is then approached along an isotherm by increasing the inlet stagnation pressure and two additional cases are investigated at 120 bar and 140 bar. The machine Mach number for all three cases is set to $M_{U2} = 0.8$, and the outlet static pressure is varied to obtain the compressor characteristic. Real gas effects become more prominent near the choke limit of the stage. A reduction of up to 9% in the choke margin and an increase of up to 5% in the swing between inlet and outlet corrected mass flow per unit area is observed. The performance parameters are normalized by their design values and presented in Figs. 8 and 9.

The very large negative incidence angle near choke conditions causes the flow to become supersonic as it accelerates around the leading edge. This effect is more prominent near the shroud as the flow turns from axial to radial. The Mach number contours along a meridional plane at 85% span, shown in Fig. 10, reveal a

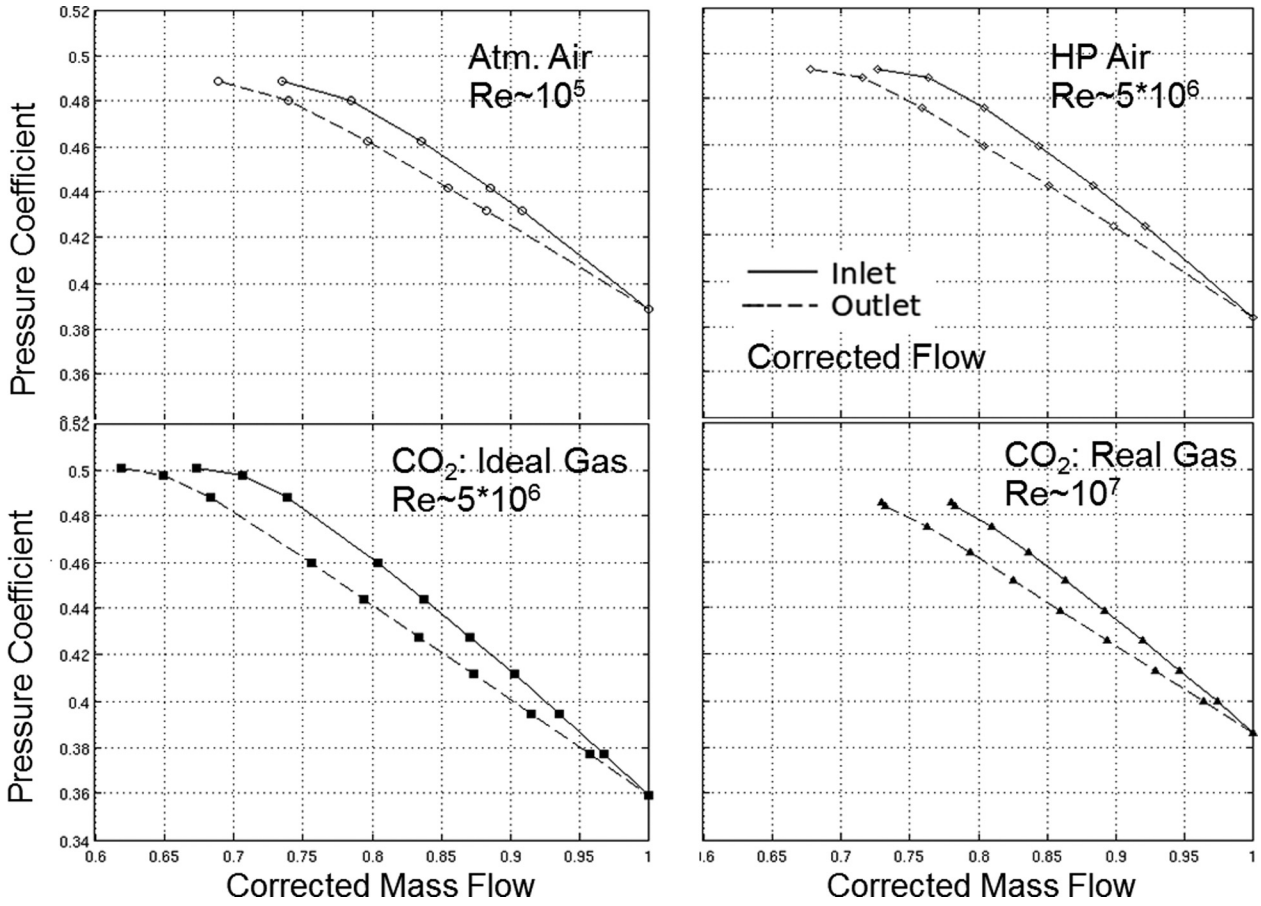

Fig. 6 Excursions in corrected mass flow from inlet to outlet of the 2D radial impeller

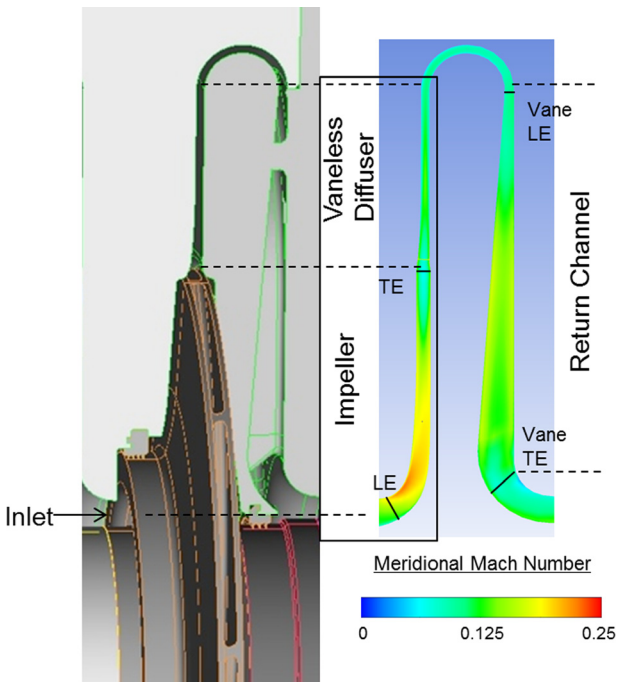

Fig. 7 Supercritical CO_2 compressor stage

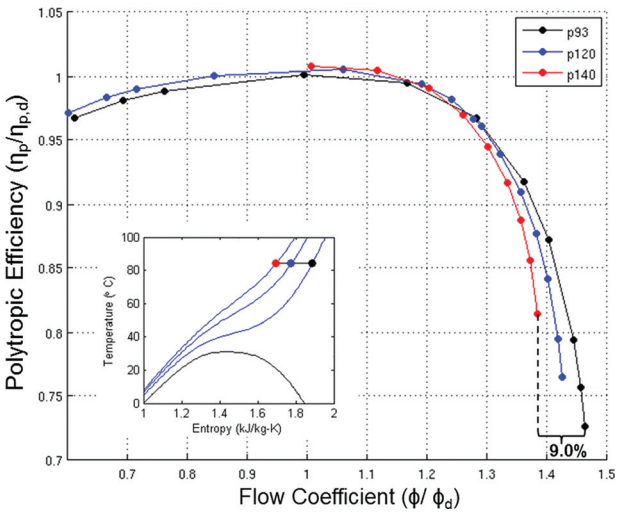

Fig. 8 Reduction in choke margin of compressor when approaching the critical point

shock-induced separation region separated from the main flow by a strong shear layer. A detailed investigation of the shear layer indicates an inflection point in the velocity profile, corresponding to a local maximum in the vorticity profile, which is a necessary condition for a Kelvin–Helmholtz type instability. While shear layers with an inflection point can be stabilized by viscosity, supercritical CO_2 compressors operate at significantly higher Reynolds numbers. Unsteady CFD simulations show weak vortices shed from the impeller trailing edge creating pressure perturbations that travel upstream and causing a disturbance in the shear layer. After just one impeller revolution, the vortex sheet rolls up and begins to shed discrete vortices as shown in Fig. 11.

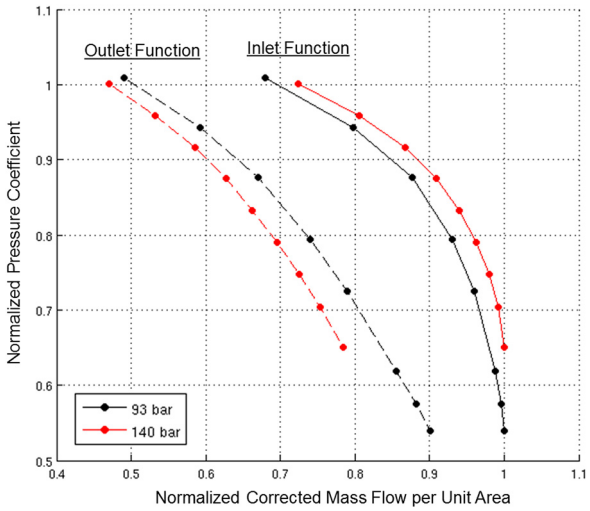

Fig. 9 Excursions in corrected mass flow per unit area between inlet and outlet of the compressor stage

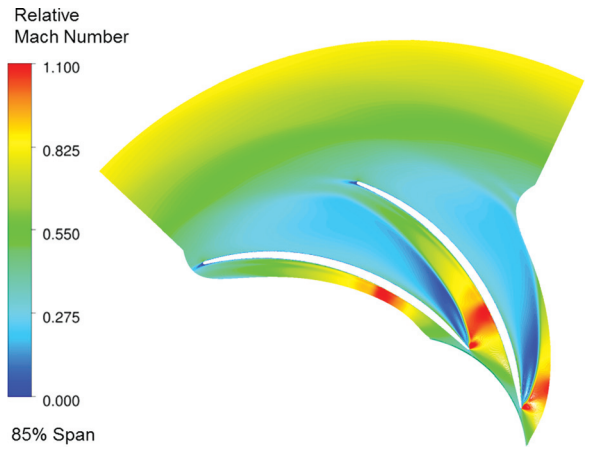

Fig. 10 Relative Mach number field at 85% span for inlet stagnation pressure of 140 bar and $\varphi/\varphi_d = 1.36$

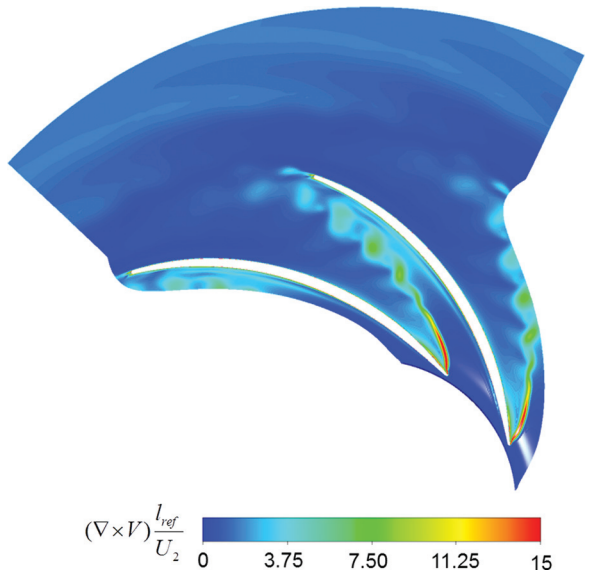

Fig. 11 Vorticity field for inlet stagnation pressure of 140 bar and $\varphi/\varphi_d = 1.36$ after one impeller revolution

Condensation Effects

The problem of condensation in turbomachinery has been studied extensively for steam turbines, where significant amount of the flow undergoes a phase change as it expands through the turbine stages. This phenomenon, however, is uncommon in compressors where the compression process occurs away from the two-phase region. Nevertheless, conditions for condensation can be attained due to the local flow acceleration near the leading edge of the impeller. In this region, the static pressure and temperature of the fluid decrease significantly and eventually fall below the saturation curve, as shown in Fig. 12.

The objectives of the present study are to establish a nondimensional criterion that determines the relative importance of two-phase flow effects in these situations and to assess the impact of condensation on the candidate compressor stage performance. This is done applying classical nucleation theory, under the assumption of nonequilibrium heterogeneous condensation.

The classical nucleation model described by McDonald [23] is commonly used to define condensation in gas turbines. The rate of nucleation is defined by

$$J = \left[\sqrt{\frac{2\sigma}{\pi m^3}}\,\frac{\rho_v^2}{\rho_l}\right] e^{\left(-\frac{\Delta G^*}{kT}\right)} \tag{14}$$

where m is the mass of a single molecule, k is the Boltzmann constant and ΔG^* represents the Gibbs free energy barrier to nucleation. The latter can be written under the assumption of spherical droplets as

$$\Delta G^* = \frac{4}{3}\pi r^{*2}\sigma \tag{15}$$

with

$$r^* = \frac{2\sigma}{\rho_l[g(p_v,T) - g(p_s,T)]} \tag{16}$$

where g is the specific Gibbs free energy and σ is the surface tension. This energy barrier is lower near solid surfaces. The free energy needed for heterogeneous nucleation can be modeled as the product of that for homogeneous nucleation and a function, f, of the contact angle θ defined as

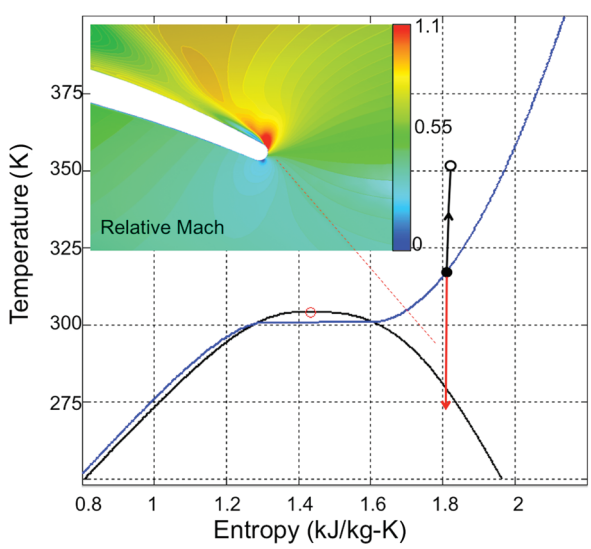

Fig. 12 Supersonic patch due to negative incidence at impeller leading edge for high flow coefficient leads to thermodynamic state below saturation

$$f(\theta) = \frac{2 - 3\cos\theta + \cos^3\theta}{4} \tag{17}$$

Because the CO_2 in the last compressor block is estimated to be 99.8%, only homogeneous condensation is considered for the bulk phase, while the heterogeneous condensation model is used near the compressor endwalls and the contact angle is assumed to be 30 deg.

Experimental evidence shows that during rapid expansion liquid droplets generally do not form at saturated conditions [24]. In fact, nucleation in high-speed flows usually occurs under subcooled conditions, which are needed to overcome the energy barrier before a spontaneous condensation leads the fluid back to nearly equilibrium conditions. The nonequilibrium state is often referred as metastable phase and is characterized by finite temperature differences and a thermodynamic relaxation loss [24].

The definition of the vapor Gibbs free energy in nonequilibrium condensation requires an estimation of the fluid properties at metastable conditions. As metastable properties have not been measured experimentally, this is usually addressed by extrapolating the gas properties onto the liquid domain. A similar technique has been used extensively in the past to model nonequilibrium condensation for water vapor in steam turbines, leading to the construction of the IAPWS-97 database [15]. However, to the authors' knowledge, no such database has been published for CO_2 at high pressures. In this study, a cubic extrapolation of the SW EOS is used to extrapolate the gas properties onto the liquid domain, as shown for example in Fig. 13, for enthalpy. Here, the spinodal limit is not marked because it is not implemented in the model. In all simulations, the thermodynamic properties of supercritical CO_2 never reach the spinodal limit.

All two-phase calculations were carried out with the commercial CFD program ANSYS CFX 14. The solver adopts two additional models for the disperse phase, a nucleation model, which determines the droplet formation, and a droplet-growth model, which describes the development of the droplet size and defines the wetness function. These models are incorporated into the mass, momentum, and energy conservation equations via source terms. The model does not assume the flow to instantaneously reach equilibrium conditions, and therefore implicitly includes losses due to thermodynamic irreversibility. The program uses an Eulerian–Eulerian approach to describe the continuous and disperse phases and solves for the gas phase variables using a coupled solution for mass and momentum. More detail of the numerical formulation is provided in Ref. [15].

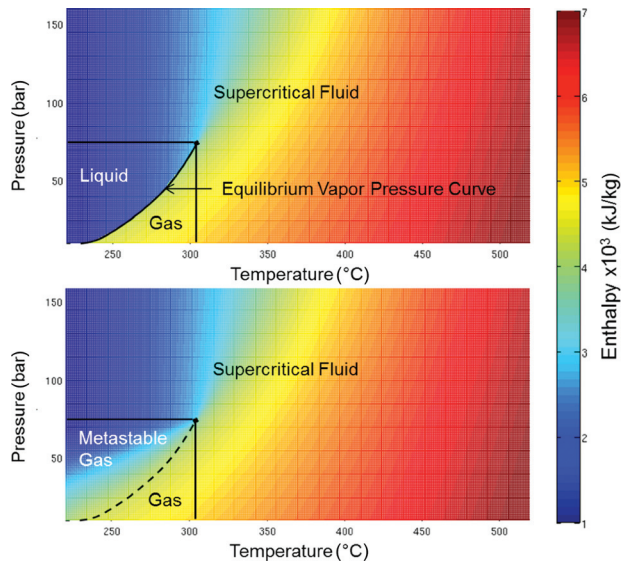

Fig. 13 Enthalpy of CO_2 based on EOS model (top) is extrapolated to define the gas property for the metastable phase (bottom)

The two-phase calculations show a negligible fraction of liquid CO_2, suggesting that condensation does not occur. It is therefore found that the computed mass fraction of condensed CO_2 is not sufficient to have an impact on the compressor performance and stability. The implication is that two-phase flow simulations are not required as long as the EOS model is amended with the metastable properties of the fluid. This is further investigated through a time scale analysis.

There are two relevant time scales that govern the condensation process. One is the time required for stable droplets to form and can be defined from the rate of nucleation as

$$t_n = \frac{1}{J_{max} V} \tag{18}$$

where V is the volume of condensing CO_2, shown in Fig. 14, and J_{max} is a volumetric nucleation frequency constructed using the maximum nucleation rate J given in Eq. (14) and the number of condensing nuclei. The other time scale is the residence time of the flow, which is defined as

$$t_r = \frac{l}{C_{ave}} \tag{19}$$

where l is the length of the condensing volume along the blade's camber line and c_{ave} is the average flow velocity.

For the candidate compressor stage at supercritical operating conditions, the time scale ratio is found to be $t_r/t_n = 0.01$, meaning that the time required for stable liquid droplets to form is significantly larger than the residence time of the flow inside the nucleating region. As a consequence, the level of supersaturation, defined as $s = P/P_v$, of the fluid is not large enough to induce significant phase change. The implication for the compressor is that condensation due to local flow acceleration around the impeller leading edge is not a concern at the current stage operating conditions.

The analysis is extended to different inlet states progressively approaching the critical point, as shown in Fig. 15. Doing so, the expansion across the saturation line becomes more significant while the surface tension of the fluid asymptotically goes to zero. This suggests a significant increase in the nucleation rate such that t_r/t_n might become unity. Moreover, the spinodal lines, which limit metastable conditions, are closer to the saturation line near the critical point, making nucleation more likely to occur. The CFD analysis shows $t_r/t_n \ll 1$ for the cases away from the critical point.

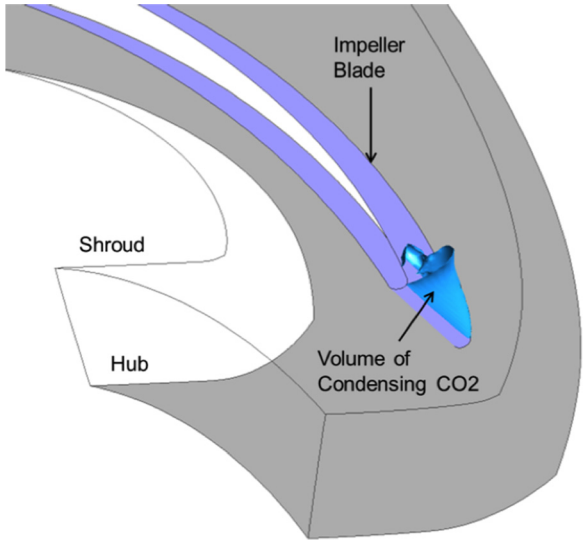

Fig. 14 Volume of metastable fluid at impeller leading edge for candidate CO_2 compressor

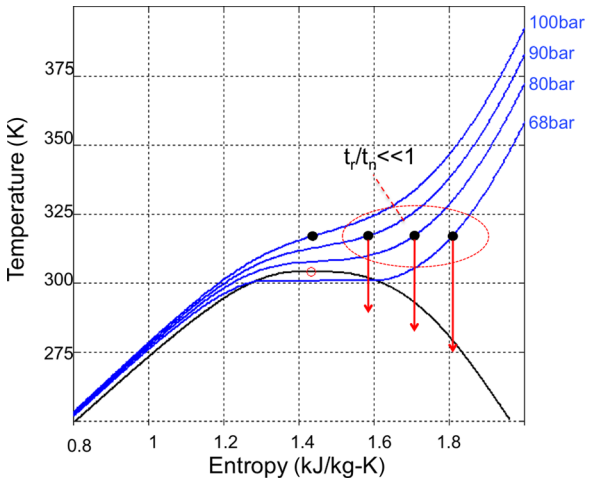

Fig. 15 Analysis of condensation approaching critical point

At the critical point, the determination of the timescales becomes challenging. Due to the increased coalescence of the molecules, Eq. (14) is expected to underestimate the nucleation rate. The accuracy of the EOS models also greatly diminishes in the proximity of the critical point, leading to larger errors. Although the CFD analysis reveals that condensation is not likely to occur due to the small residence time of the fluid relative to the nucleation time, the numerical simulation models need to be supplemented by experimental measurements. This is the objective of current work, where a laboratory scale experiment is being conducted to investigate real gas effects and condensation of supercritical CO_2 near the critical point.

Summary and Conclusions

This paper presents a comprehensive assessment of real gas effects in supercritical CO_2 compressors. While the main focus is on investigating the root cause for performance and stability issues near the critical point, the proposed framework serves as a foundation for the advanced studies of the internal flow behavior of real fluids.

A qualitative analysis from first principles is used to identify potential mechanisms for performance and stability deterioration before conducting numerical simulations to quantify their effects on a candidate centrifugal compressor stage representative of typical CCS and EOR compressors. The compressible flow relations and the influence coefficients for one-dimensional real gas channel flow were derived. These were used to assess trends in the gas dynamic behavior of real fluids, such as the inversion of gas dynamic effects and the variations in corrected mass flow per unit area. The behavior of real gas properties, such as the compressibility factor Z and the isentropic exponent n_s, was examined to identify the thermodynamic conditions where real gas effects are expected to be prominent.

It is found that in the range of typical S-CO_2 compressor operating conditions the fundamental derivative remains positive, implying that inversion of gas dynamic effects is not a concern. Approaching the critical point, the compressor choke margin is reduced by 9% due to the increase in the isentropic exponent. Furthermore, the excursion in corrected mass flow per unit area increases by 5% impacting the matching of downstream components. Moreover, at high flow coefficients, the local flow acceleration around the impeller leading edge causes the thermodynamic conditions to fall below the vapor-pressure curve. A nondimensional criterion was established that determines whether condensation might occur. This criterion relates the time required for stable liquid droplets to form, which depends on the expansion through the vapor-pressure curve, and the residence time of the flow under saturated conditions. Two-phase flow effects can be considered negligible when the ratio of the two time scales is much smaller than unity. Two-phase calculations of a candidate compressor revealed that the nucleation time scale ratio is indeed much smaller than unity for the operating conditions characteristic of CCS compressors, indicating that condensation is not a concern.

While the variation in real gas properties and the flow expansion through the vapor-pressure curve are assessed independently in this study, both mechanisms are expected to be more prominent in the immediate vicinity of the critical point. Numerical simulations were used to investigate their simultaneous effect on the compressor performance. However, the singular behavior of thermodynamic properties at the critical point prevents the numerical schemes from capturing important gas dynamic effects. The classical nucleation theory, on the other hand, might not provide an accurate description of the phase change processes occurring in this region. These limitations require experimental assessment. As such a laboratory scale experiment with supercritical CO_2 is currently underway to validate the concepts and methods presented in this paper and to support the modeling capabilities in the vicinity of the critical point.

Acknowledgment

This research was funded by Mitsubishi Heavy Industries Takasago R&D Center which is gratefully acknowledged. In particular, the authors would like to thank Dr. Sumiu Uchida, Dr. Eisaku Ito, and Mr. Akihiro Nakaniwa for their support and for providing experimental data.

Nomenclature

a = speed of sound
A = area
b_2 = impeller width
c = velocity
c_p = isobaric specific heat capacity
c_v = isochoric specific heat capacity
d_2 = impeller diameter
g = specific Gibbs free energy
G = Gibbs free energy
h = specific enthalpy
h^+_s = equivalent sand grain roughness
J = nucleation rate
k = Boltzmann's constant
l = length scale
m = molecular mass
M = Mach number, $U_2/a_{t,0}$
$\dot{m}$ = mass flow rate
m_s = isentropic temperature exponent
M_{U2} = machine Mach number
n = polytropic exponent
n_s = isentropic pressure exponent
p = pressure
r = radius
R = gas constant
Re = stage Reynolds number, $(U_2 b_2)/\nu_{t,0}$
s = entropy
T = temperature
t_n = nucleation time
t_r = residence time
u = specific internal energy
U_2 = impeller tip speed
v = specific volume
V = volume
w_p = specific polytropic work
Z = compressibility factor
β_p = isobaric compressibility
β_T = isothermal compressibility
γ = ratio of specific heats

Γ = fundamental derivative
η_p = polytropic efficiency
θ = contact angle
μ_p = pressure coefficient
ν = kinematic viscosity
ρ = density
σ = surface tension
φ = flow coefficient, $\dot{m}/(\pi\rho_{t,0}U_2(d_2/2)^2)$

Appendix

The thermodynamic properties of CO_2 represented on the *T-s* diagrams shown in Figs. 16–21 are obtained with the LK EOS. The range of thermodynamic states is between 15 bar and 700 bar in pressure and from −25 °C to 200 °C in temperature. The isobars and the isenthalps are kept the same in all diagrams. Additional diagrams can be found in Ref. [17].

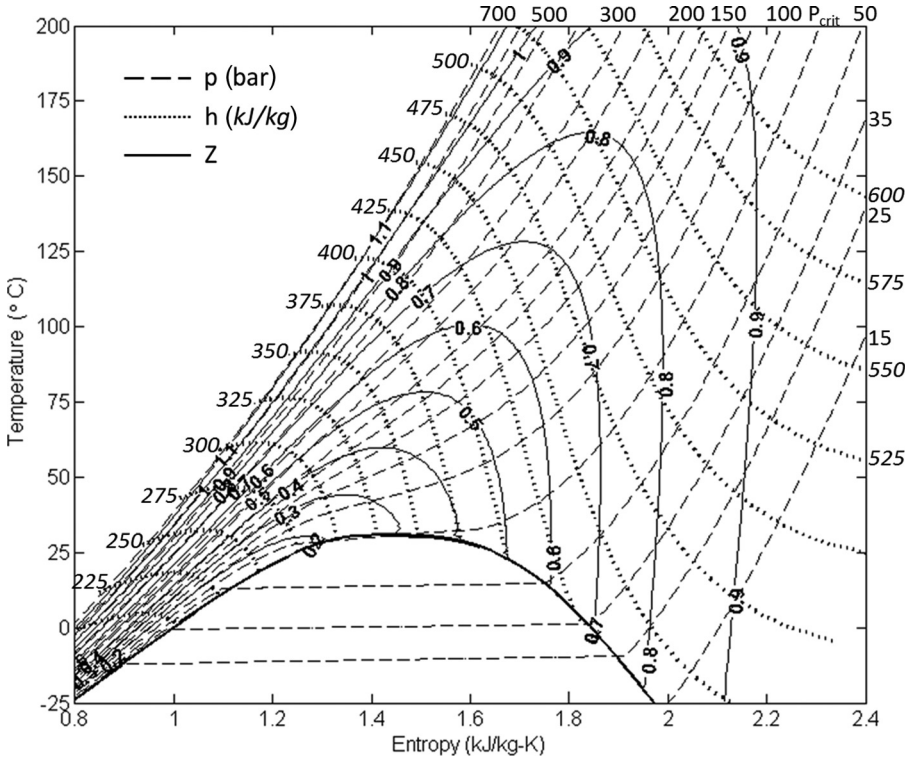

Fig. 16 Contours of compressibility factor

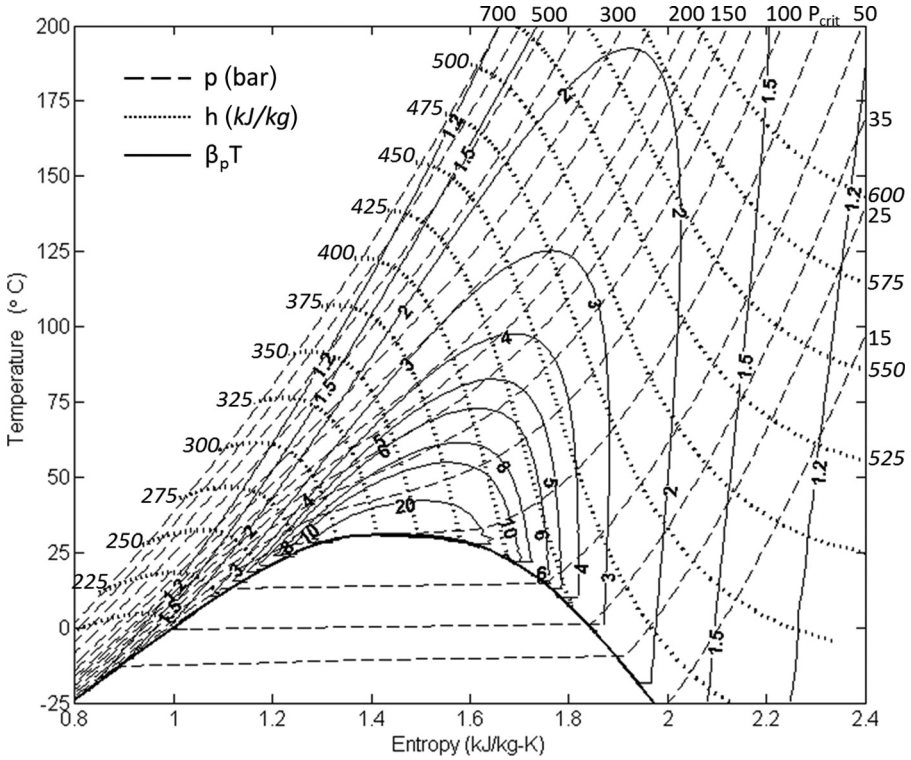

Fig. 17 Contours of compressibility function $\beta_p T$

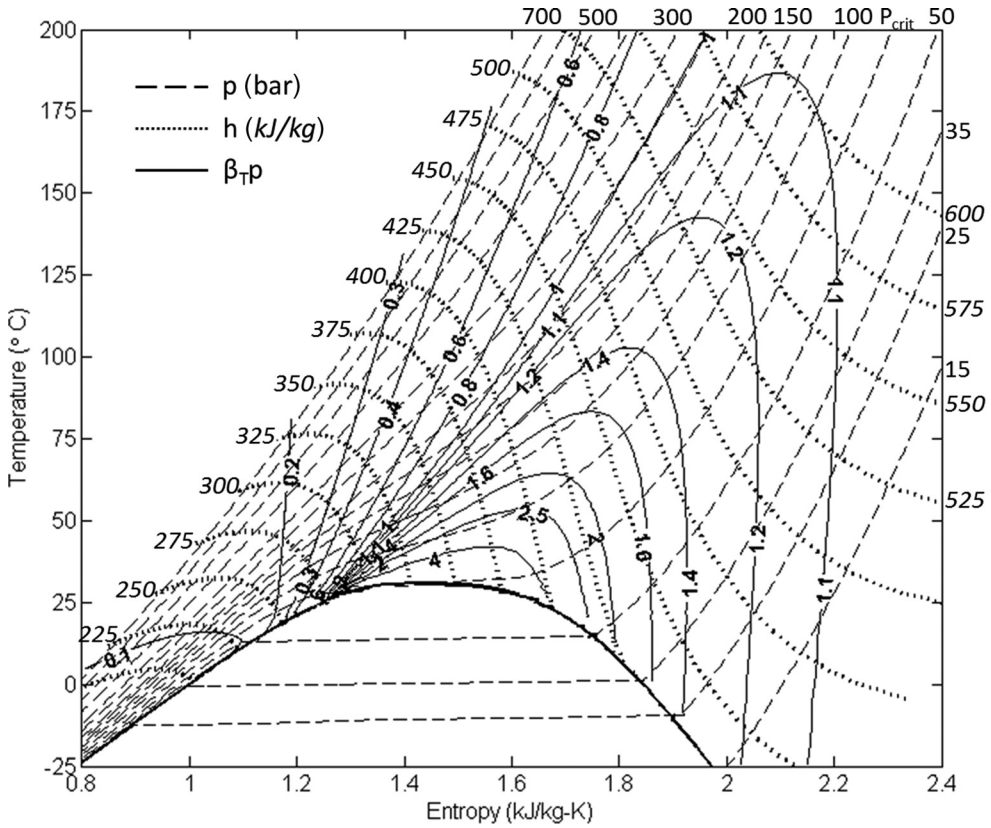

Fig. 18 Contours of compressibility function $\beta_T p$

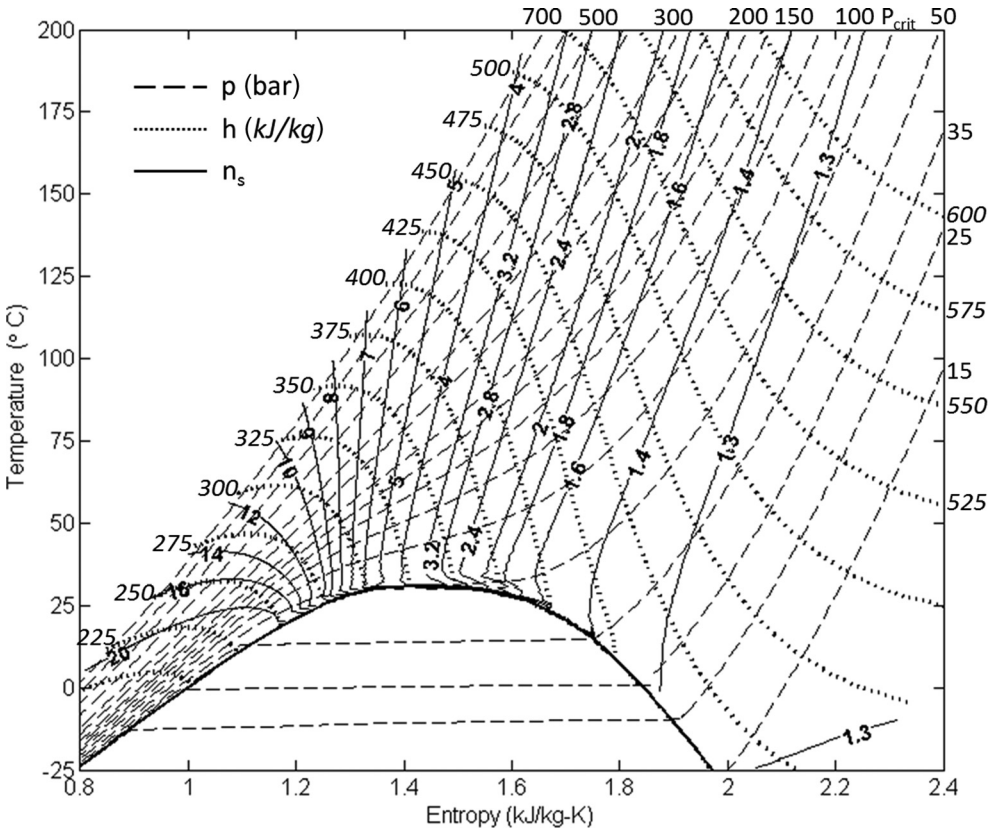

Fig. 19 Contours of isentropic pressure exponent n_s

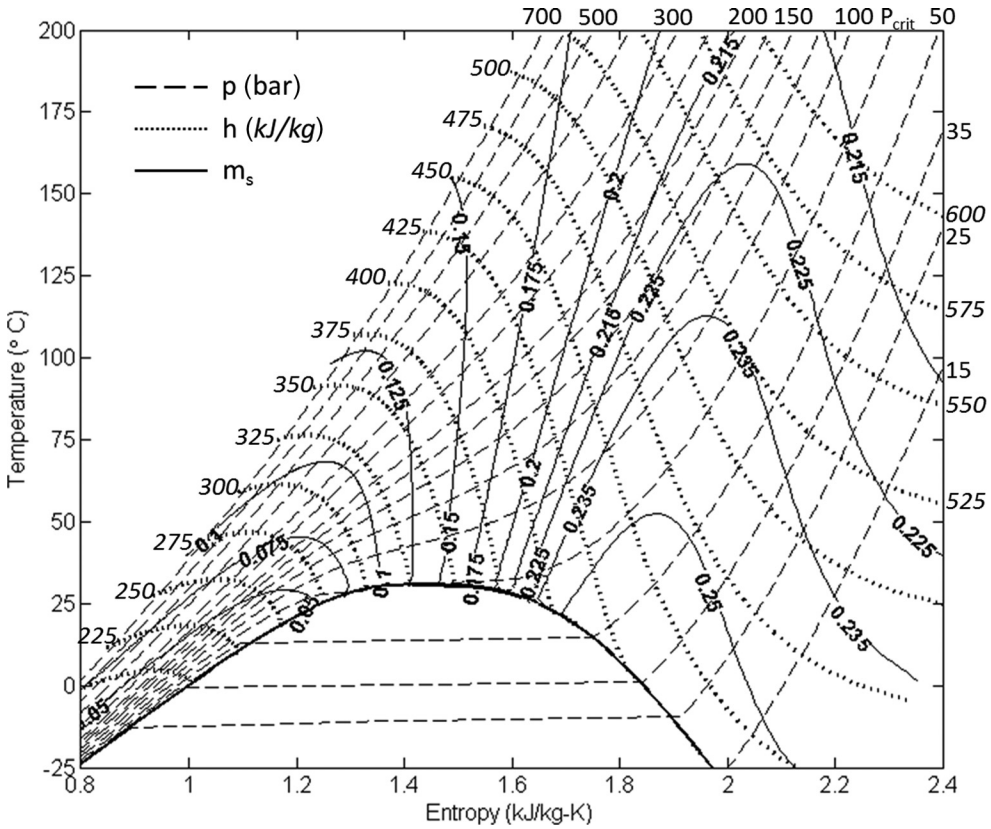

Fig. 20 Contours of isentropic pressure exponent m_s

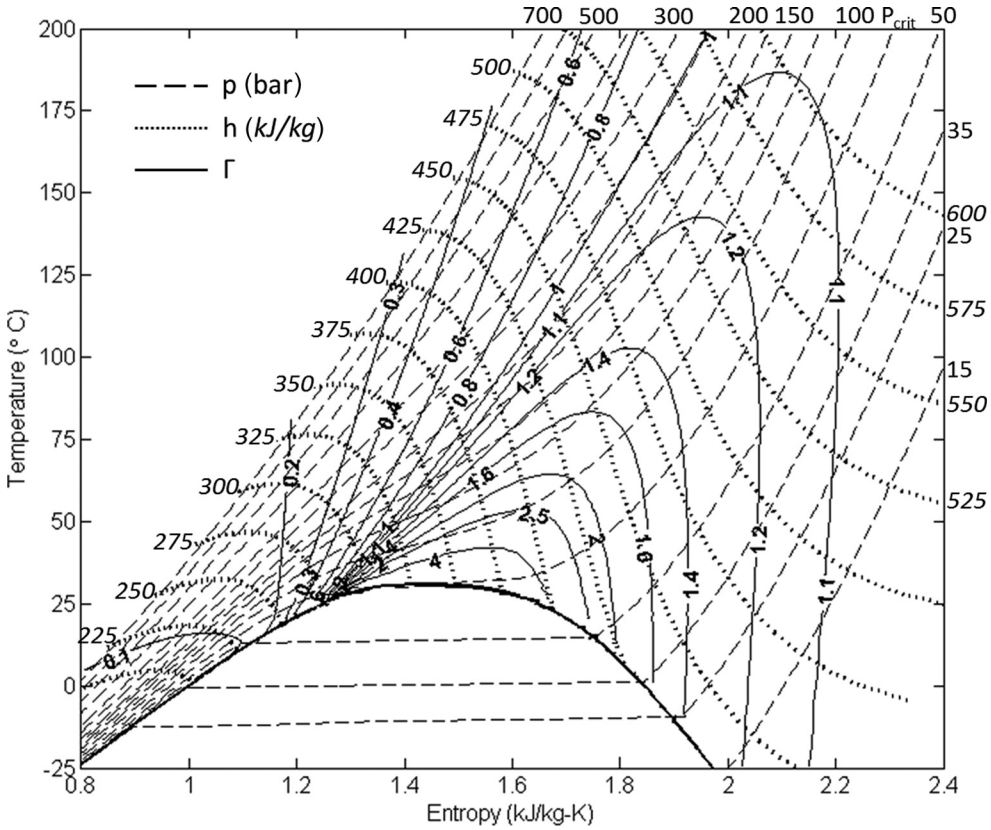

Fig. 21 Contours of fundamental derivative

References

[1] U.S. EPA, 2012, "Inventory of U.S. Greenhouse Gas Emissions and Sinks: 1990–2012," U.S. Environmental Protection Agency, Washington, DC, Technical Report No. 430-R-14-003.

[2] Kobayashi, S., and Van Hassel, B., 2005, "CO_2 Reduction by Oxy-Fuel Combustion: Economics and Opportunities," Global Climate and Energy Project (GCEP) Advanced Coal Workshop, Provo, UT, Mar. 15–16.

[3] Wright, S., Radel, R., Vernon, M., Rochau, G., and Pickard, P., 2010, "Operation and Analysis of a Supercritical CO_2 Brayton Cycle," Sandia National Laboratories, Albuquerque, NM, Technical Report No. SAND2010-0171.

[4] Lettieri, C., Baltadjiev, N., Casey, M., and Spakovszky, Z., 2014, "Low-Flow-Coefficient Centrifugal Compressor Design for Supercritical CO_2," ASME J. Turbomach., **136**(8), p. 081008.

[5] Lüdtke, K. H., 2003, *Process Centrifugal Compressors*, Springer, New York, Chap. 2.

[6] Span, R., and Wagner, W., 1996, "A New Equation of State for Carbon Dioxide Covering the Fluid Region From the Triple-Point Temperature to 1100 K at Pressures up to 800 MPa," J. Phys. Chem. Ref. Data, **25**(6), pp. 1509–1596.

[7] Moore, J. J., and Nored, M. G., 2008, "Novel Concepts for the Compression of Large Volumes of Carbon Dioxide," ASME Paper No. GT2008-50924.

[8] Moore, J. J., Lerche, A., Allison, T., Moreland, B., and Pacheco, J., 2012, "Development of an Internally Cooled Centrifugal Compressor for Carbon Capture and Storage Applications," ASME Paper No. GT2012-69911.

[9] Kimball, K. J., and Clementoni, E. M., 2012, "Supercritical Carbon Dioxide Brayton Power Cycle Development Overview," ASME Paper No. GT2012-68204.

[10] Conboy, T., Wright, S., Pasch, J., Fleming, D., Rochau, G., and Fuller, R., 2012, "Performance Characteristics of an Operating Supercritical CO_2 Brayton Cycle," ASME J. Eng. Gas Turbines Power, **134**(11), p. 111703.

[11] Turchi, C. S., Ma, Z., and Dyreby, J., 2012, "Supercritical Carbon Dioxide Power Cycle Configurations for Use in Concentrating Solar Power Systems," ASME Paper No. GT2012-68932.

[12] Fuller, R., Noall, J., and Preuss, J., 2012, "Turbomachinery for Supercritical CO_2 Power Cycles," ASME Paper No. GT2012-68735.

[13] Lee, J., Ahn, Y., Lee, J. I., and Yoon, H., 2012, "Design Methodology of Supercritical CO_2 Brayton Cycle Turbomachineries," ASME Paper No. GT2012-68933.

[14] Pecnik, R., Rinaldi, E., and Colonna, P., 2012, "Computational Fluid Dynamics of a Radial Compressor Operating With Supercritical CO_2," ASME J. Eng. Gas Turbines Power, **134**(12), p. 122301.

[15] ANSYS Academic Research, Release 14.5, Theory Manual, ANSYS, Inc, Canonsburg, PA.

[16] Lemmon, E. W., Huber, M. L., and McLinden, M. O., 2010, "NIST Standard Reference Database 23: Reference Fluid Thermodynamic and Transport Properties—REFPROP, Version 9.0," National Institute of Standards and Technology, Standard Reference Data Program, Gaithersburg, MD.

[17] Baltadjiev, N., 2012, "An Investigation of Real Gas Effects in Supercritical CO_2 Compressors," Master's thesis, Massachusetts Institute of Technology, Cambridge, MA.

[18] Greitzer, E. M., Tan, C. S., and Graf, M. B., 2004, *Internal Flow Concepts and Applications*, Cambridge University Press, New York.

[19] Cheng, D., Fan, X., and Yang, M., 2012, "Quasi-1D Compressible Flow of Hydrocarbon Fuel," 48th AIAA/ASME/ SAE/ASEE Joint Propulsion Conference & Exhibit, Atlanta, July 29–Aug. 1, AIAA Paper No. 2012-4090.

[20] Thompson, P., 1971, "A Fundamental Derivative in Gas Dynamics," Phys. Fluids, **14**(9), pp. 1843–1849.

[21] Schultz, J., 1985, "Polytropic Analysis of Centrifugal Compressors," ASME J. Eng. Gas Turbines Power, **84**(1), pp. 69–82.

[22] Sonntag, R., Borgnakke, C., and Van Wylen, G., 2002, *Fundamentals of Thermodynamics*, 6th ed., Wiley, New York.

[23] McDonald, J. E., 1962, "Homogeneous Nucleation of Vapour Condensation. I. Thermodynamic Aspects," Am. J. Phys., **30**(12), pp. 870–877.

[24] Gyarmathy, G., 2005, "Nucleation of Steam in High-Pressure Nozzle Experiments," J. Power Energy, **219**(6), pp. 511–521.